

First-principles calculation of elastic moduli of early-late transition metal alloys

William Paul Huhn and Michael Widom

Department of Physics, Carnegie Mellon University, Pittsburgh, Pennsylvania 15213, USA

Andrew M. Cheung and Gary J. Shiflet

Department of Materials Science and Engineering, University of Virginia, Charlottesville, Virginia 22904, USA

S. Joseph Poon

Department of Physics, University of Virginia, Charlottesville, Virginia 22904, USA

John Lewandowski

Department of Materials Science and Engineering, Case Western Reserve University, Cleveland, OH 44106, USA

(Received 25 October 2013; published 6 March 2014)

Motivated by interest in the elastic properties of high-strength amorphous metals, we examine the elastic properties of select crystalline phases. Using first-principles methods, we calculate elastic moduli in various chemical systems containing transition metals, specifically early (Ta,W) and late (Co,Ni). Theoretically predicted alloy elastic properties are verified for Ni-Ta by comparison with experimental measurements using resonant ultrasound spectroscopy. Comparison of our computed elastic moduli with effective medium theories shows that alloying leads to enhancement of bulk moduli relative to averages of the pure elements and considerable deviation of predicted and computed shear moduli. Specifically, we find an enhancement of bulk modulus relative to effective medium theory and propose a candidate system for high-strength, ductile amorphous alloys. Trends in the elastic properties of chemical systems are analyzed using force constants, electronic densities of state, and crystal overlap Hamilton populations. We interpret our findings in terms of the electronic structure of the alloys.

DOI: [10.1103/PhysRevB.89.104103](https://doi.org/10.1103/PhysRevB.89.104103)

PACS number(s): 62.20.de, 31.15.A–, 61.43.Dq, 71.20.Be

I. INTRODUCTION

Elastic moduli are important for understanding various properties of amorphous metals. Bulk moduli, shear moduli, and their ratio correlate to glass transition temperature [1,2], glass forming ability [3], brittleness [4–6], Grüneisen parameters [7], maximum resolved shear stress at yielding [8], chemical bonding type [9], and possibly fragility [9]. Knowledge of the bulk and shear moduli is thus important for materials design. However, amorphous materials commonly contain at least four chemical species, making exhaustive experimental evaluation of candidate materials impossible. Empirical methods for predicting stoichiometries with desired properties are therefore necessary.

First-principles computational methods prove fruitful, owing to their chemical specificity and absence of adjustable parameters, as well as the insight they yield into electronic structure. However, amorphous metals pose computational difficulties, as they lack both spatial periodicity and a unique structure. While the first problem can be practically overcome by imposing suitably large periodic boundary conditions, this requires hundreds of atoms per computational cell, straining computational resources, and requiring averaging over multiple samples to remove sample dependence. The second problem can be partially overcome by running molecular dynamics on a liquid sample then rapidly quenching the sample. However, the requirement for equilibration further increases the computational time necessary. Hence we adopt a different strategy.

Frank Kasper phases [10–12] are complex but otherwise ordinary crystalline phases. Due to their topological close

packing they exhibit local icosahedral ordering similar to that found in many amorphous metals. Figure 1 shows the standard Voronoi polyhedra of Frank-Kasper structures. We expect that the similar local chemical environments of the Frank-Kasper phases can be used to mimic amorphous metals, yielding “amorphous approximants,” similar in concept to “quasicrystal approximants.” These crystalline phases will be used to understand trends in the elastic properties of amorphous metals. It is observed that in amorphous metals, shear moduli are typically 20%–30% lower, and bulk moduli 5%–10% lower, compared to crystalline phases of similar composition [5]. Many crystalline phases have small unit cells compared to system sizes required to reproduce amorphous structures.

Amorphous metals can exhibit high strength [13], but often at the cost of a lack of ductility owing to the absence of dislocations. Designing amorphous alloys for high ductility is impeded both by the challenge of formulating accurate amorphous structural models, and by the lack of a valid predictive theory of ductility even for the case of crystalline compounds, though there are empirical rules based on the Poisson ratio, or equivalently the shear/bulk modulus ratio. We hypothesize that relatively ductile crystalline compounds will tend to create relatively ductile amorphous compounds. Further, metallic glass composites, consisting of crystalline grains embedded in an amorphous matrix, have been shown to increase the toughness, impact resistance and plastic strain to failure [14], further motivating the investigation into elastic properties of crystalline phases in metallic glass-forming alloy systems.

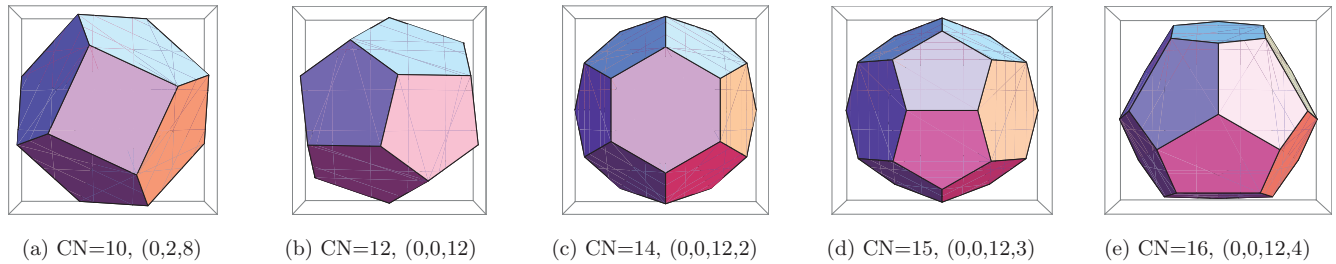


FIG. 1. (Color online) Frank-Kasper Voronoi polyhedra, listing coordination numbers and polyhedron codes.

II. BACKGROUND AND METHODS

A. Elasticity

The fundamental equation of linearized elasticity is $\sigma_i = C_{ij}\epsilon_j$, where σ is the stress tensor, ϵ is the strain tensor, and C the stiffness tensor relating the two. Here, we employ Voigt notation, converting the tensors σ and ϵ into vectors with 6 components $\{xx,yy,zz,xy,xz,yz\}$. For crystals, C depends on the symmetry of the material in question [15] and contains at least three independent parameters. For the special case of isotropic materials, C has only two independent parameters, the bulk modulus K and the shear modulus G . The nonvanishing elements are $C_{11} = C_{22} = C_{33} = K + 4G/3$, $C_{12} = C_{13} = C_{23} = K - 2G/3$, and $C_{44} = C_{55} = C_{66} = G$. An additional elastic quantity of interest is the Poisson ratio ν , defined to be the negative of the ratio of transverse strain to axial strain. For crystals, ν depends on the direction of applied stress, but in the isotropic case, it reduces to

$$\nu = \frac{3 - 2G/K}{6 + 2G/K}. \quad (1)$$

Notice that ν is a function of the shear to bulk modulus ratio G/K , also known as the Pugh ratio [16].

Ductility and Poisson's ratio are positively correlated in both polycrystalline [16] and amorphous [4] solids, with $\nu \geq 0.32$ (equivalently $G/K \leq 0.41$) proposed as an empirical criterion for good ductility [17]. Seeking simultaneously high strength and ductility, it is natural to choose chemical species which in elemental form have large K . The species chosen must also be known good glass formers. Early-late transition metal alloys fit both criteria, as the transition metals from group IV to XI all have $K \geq 100$ GPa, and they are one of the most frequently examined classes of amorphous metals. Size mismatch criteria favor using transition metals from different rows and columns of the periodic table, e.g., Ta and W for early transition metals (ETMs), and Co and Ni as late transition metals (LTMs). Co and W are of particular interest for materials design as Co-based glasses exhibit ultrahigh fracture strength, W-based glasses have the highest known glass transition temperature for bulk metallic glasses, and both have high Young's modulus [9,18,19].

Ordinary crystalline materials contain randomly orientated microscopic grains and appear macroscopically isotropic. To compute the elastic properties for these "polycrystals," orientational averaging is required. Each grain is described microscopically by the same stiffness matrix, which contains between three (cubic) and 21 (triclinic) independent parameters [20], but macroscopically the crystal is isotropic with only

two independent parameters K and G . In the Voigt average, the stiffness matrix C is averaged over orientations [21], which is exact if stress is uniform throughout space. In the Reuss average, the compliance matrix $S = C^{-1}$ is averaged over orientations, which is exact if strain is uniform throughout space. The Voigt average systematically overestimates the isotropic moduli, while the Reuss average systematically underestimates the moduli. Empirically, the arithmetic mean of the two, known as the Hill average [22], gives improved agreement with experiment, and this is what we will report.

The polycrystalline average assumes the stiffness matrices of various grains are identical to the perfect crystal, differing only by relative orientation. To obtain macroscopic elastic moduli in materials where chemical environment spatially varies, in particular, in materials containing chemically distinct grains, it is necessary to include effects arising from fluctuations in the local stiffness matrices. A general class of approximation schemes known as "effective medium theories" exists where each grain with its local stiffness matrix interacts with an effective medium characterized by a background stiffness matrix incorporating the interactions of all other grains. A popular effective medium theory is the coherent potential approximation (CPA) [23], a self-consistent formalism in which the background stiffness matrix is taken as the macroscopic average itself. The self-consistent interaction of grains yields a pair of coupled nonlinear equations,

$$\sum_i \phi_i \frac{K_i - K}{3K_i + 4G} = 0 \quad (2)$$

and

$$\sum_i \phi_i \frac{G_i - G}{5G(3K + 4G) + 6(K + 2G)(G_i - G)} = 0, \quad (3)$$

which can be solved numerically for the effective K and G , where ϕ_i denotes the volume fraction of grain type i in the material. K_i and G_i denote the bulk and shear modulus of grain type i , respectively.

Although intended for mixtures of crystalline grains, we will apply CPA in the limit where each grain shrinks to a single atom, to estimate the elastic moduli of compounds using the self-consistent average of properties of the constituent pure elements. Our usage of CPA may be viewed as a higher-order correction to the well-known but highly empirical "rule of mixtures" paradigm common in materials design, which has already been applied to bulk metallic glasses [24]. CPA takes into account the pure elemental properties but lacks information about interspecies bonding and specific alloy crystal structure. Thus we take CPA as a convenient,

physically motivated interpolation to establish a baseline for comparison with the computed alloy moduli revealing the specific contributions of structure and bonding, though we note that metallic glasses exist where trace changes in composition yield relatively large changes in K and G due to alteration of chemical bonding type [25].

B. First-principles methods

Our first-principles calculations use the Vienna *ab initio* simulation package (VASP) [26,27], a plane-wave *ab initio* package implementing PAW pseudopotentials [28] in the PW91 [29] generalized gradient approximation to density functional theory (DFT). VASP calculates total energies, forces, elastic moduli, and electronic structure. All structures are relaxed until the maximum ionic force is below 0.01 eV/Å, and the k -point density is subsequently increased until total energy per atom has converged to within 0.1 meV/atom. Default plane wave energy cutoffs are used for total energy calculations. In structures containing Co and Ni, spin polarization has been included. However, we do not include spin-orbit coupling despite the presence of 5d elements Ta and W. Total energies are converted to enthalpies of formation by subtracting from the tie-line joining the total energies of pure elements in their stable crystalline forms [30].

We perform elastic calculations using a finite difference method internal to VASP. To ensure proper convergence of elastic moduli, we increase the k -point density until the all polycrystalline averages converge to within 2%, then increase the energy cutoff until the polycrystalline averages converge. Convergence in energy cutoff occurs at 360 eV, with the exception of Ni₂Ta and Ni₄W where 400 and 440 eV, respectively, were required. All structures were tested for mechanical stability, and elastic constants were not calculated for structures that were found to be mechanically unstable, though they were included in the enthalpy of formation plots, as it is possible for the stabilizing distortions to affect the calculated total energy only weakly.

To quantify bond strength between individual atoms in structures, we calculate interatomic force constants and the crystal overlap Hamilton population (COHP). To calculate the force constant $k_{\alpha\beta}$ between atoms α, β at position $\vec{r}_{\alpha,\beta}$, separated by a bond in the direction $\hat{\gamma}_{\alpha\beta}$, we calculate the Hessian matrix $\mathbf{H}_{\alpha\beta} = d^2E/d\delta\vec{r}_{\alpha}d\delta\vec{r}_{\beta}$. We use density functional perturbation theory internal to VASP to calculate \mathbf{H} within a supercell of sufficient size that atoms lie at least 4.2 Å away from their own repeated images. Restricting our attention to longitudinal (bond stretching) interactions and assuming central forces, we define

$$k_{\alpha\beta} \equiv \hat{\gamma}_{\alpha\beta} \cdot \mathbf{H}_{\alpha\beta} \cdot \hat{\gamma}_{\alpha\beta} \quad (4)$$

as the projection of the Hessian along $\hat{\gamma}_{\alpha\beta}$. $k_{\alpha\beta}$ must be positive for the force to be stabilizing.

The COHP provides an electronic structure-based characterization of interatomic bond strength [31]. One calculates matrix elements $\langle \alpha L | H | \beta L' \rangle$ of the density functional theory Hamiltonian between localized atomic orbitals L and L' on a pair of atoms α and β , then multiplies by the density of states $N_{\alpha L, \beta L'}$ projected onto the two orbitals. We calculate wave functions using a TB-LMTO method [32] then calculate

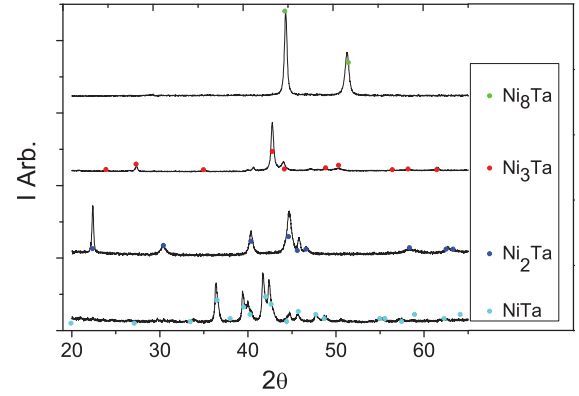


FIG. 2. (Color online) XRD verification of single phases of Ni₈Ta, Ni₃Ta, Ni₂Ta, and NiTa.

an *integrated* COHP for a pair of atoms $\alpha\beta$, summing over atomic orbitals and integrating over energies up to the Fermi energy.

C. Experimental methods

To check the validity of our first-principles calculations, we have prepared samples of single phase alloys of Ni-Ta by arc melting the pure element constituents (Ni 99.995% and Ta 99.95%) under an argon atmosphere. The alloys were then suction cast into water cooled copper molds to form rods of 2-mm diameter. Single phases of the rod samples were verified by x-ray powder diffraction (XRD) (Fig. 2). Cylindrical samples were obtained by sectioning the rods with a diamond saw into 4-mm segments. The ends of the segments were polished to a 3-μm finish. The elastic constants of the cylinders were calculated using data obtained from a Magnaflux Quasar resonant ultrasound spectrometer (RUS). RUS involves placing the cylindrical samples diagonally between two ultrasonic transceivers and recording the natural modes of vibration [33]. A Levenberg-Marquardt algorithm is then used to determine the elastic constants by finding the best fit solution through minimization of the difference between measured and calculated natural modes through iterative changes to the values of elastic constants.

The RUS measurement technique is limited to nonmagnetic samples. The study using the RUS measurements for comparison to theory is limited to the Ni-Ta system where single phases of Ni₈Ta, Ni₃Ta, Ni₂Ta, and NiTa, which are nonmagnetic, can be produced, allowing for RUS measurements. Rods of the pure elements Ni and Ta can also be cast, but of the two only Ta produces nonmagnetic rods.

III. RESULTS

In this section, we first discuss atomistic structure, then present results on thermodynamic stability for each alloy system considered, finally we address the elastic moduli.

A. Structure

Because we consider a large number of specific structures, we establish a numbering scheme to unambiguously identify

TABLE I. Structure types considered listing common prototype, and Strukturbericht and Pearson notations. Frank-Kasper phases list common names. “*” indicates symmetry-breaking distortion. “Non-FK” indicates noncanonical Frank-Kasper phase containing CN = 10 Bernal Hole. The final column contains a list of coordination numbers from Voronoi polyhedra appearing in the structure [34,36,37].

Ref.	Prototype	Strukt.	Pearson	FK?	CN
1	Cu	A1	cF4	NA	12
2	W	A2	cI2	NA	14
3	Mg	A3	hP2	NA	12
4	Fe ₆ W ₇	D8 ₅	hR13	μ	12, 14, 15, 16
5	Al ₂ Cu	C ₁₆	tI12	non-FK	10, 15
6	AuCu ₃	L1 ₂	cP4	NA	12, 18
7	BaPb ₃		hR12	NA	12, 18
8	MgNi ₂	C36	hP24	Laves	12, 16
9	MgZn ₂	C14	hP12	Laves	12, 16
10	MgCu ₂	C15	cF24	Laves*	12, 16
11	Ni ₃ Sn	D0 ₁₉	hP8	NA	12, 18
12	Al ₃ Ti	D0 ₂₂	tI8	NA	12, 14, 16
13	Cu ₃ Ti	D0 ₈	oP8	NA	12, 14, 16
14	NbPt ₃		mP16	NA	12, 14, 16
15	MoSi ₂	C11 _b	tI6	NA	14
16	MoNi ₄	D1 _a	tI10	NA	13, 14
17	Pt ₈ Ti		tI18	NA	13, 14
18	MoNi		oP56	δ	12, 14, 15, 16

them (see Table I). In the text, we refer to a given crystalline material using the notation compound.pearson (e.g., Co₂Ta.cF24). Of particular interest are the Frank-Kasper structures, which we take as amorphous approximants owing to the prevalence of their coordination polyhedra in many metallic glasses [34,35]. Canonical Frank-Kasper polyhedra have coordination numbers CN = 12, 14, 15 and 16. However, we include the Bernal holes [36,37], notably CN = 10, as tetrahedral but noncanonical Frank-Kasper polyhedra [34] suitable for smaller atoms. Also, the tetrahedral close packing of the Frank Kasper phases matches the packing properties expected in bulk metallic glasses [38].

To justify use of crystalline phases as amorphous approximants, we compare Honeycutt-Andersen common neighbor statistics [39,40], of crystalline and amorphous structures. Amorphous structures were simulated by quenching 100 atom liquid structures in NPT ensembles from $T = 2500$ K down

to 300 K over runs of more than 15 ps. All simulations were performed at the gamma point with default energy cutoffs. Shown in Fig. 3 is the number of common neighbors between two bonded atoms of given types. We show results for Co-Ta, but Ni-Ta, Ni-W, and Co-W were also simulated and generated similar results, with the exception of one Ni-W amorphous sample which was likely out of equilibrium.

All structures have many bonds with $n = 5$ common neighbors, especially between unlike atomic species, reflecting the prevalence of icosahedral ordering in Frank-Kasper phases and amorphous materials. Very few Co-Co bonds have $n = 6$ common neighbors, and very few Ta-Ta bonds have $n = 4$ common neighbors, reflecting the relative sizes of Co and Ta atoms. Because hR13 is a canonical Frank-Kasper phase with no bonds sharing $n = 4$ common neighbors, we utilize tI12 to capture the role of $n = 4$ Co-Co bonds.

B. Stability

Figure 4 summarizes our calculated enthalpies of formation. Vertices of the convex hull of enthalpy as a function of composition are predicted to be stable phases at low temperature [30]. We employ special plotting symbols to indicate phases claimed experimentally to be stable at low temperature (heavy circles) and high temperature (light circles). Phases whose stability or existence is in question are shown as squares. From the prevalence of heavy circles on or near the convex hull, we see general (though imperfect) agreement with the experimentally reported phase diagrams. We briefly summarize our findings for the four alloy systems of primary interest.

1. Co-Ta

For Co-Ta [Fig. 4(a)], at $x = 0.25$, we find that cP4 and hR12 (reference numbers 6 and 7) are nearly degenerate, with cP4 (stability not reported experimentally) favored by 1 meV/atom, which is closer than DFT can reliably distinguish. At $x = 0.33$, three different Laves phases have been reported (reference Nos. 8–10), with conflicting claims of stability and uncertain composition. We find that none of these phases lies on the convex hull. Further, all of their structures are mechanically unstable to deformation, casting doubt on the reported structure and stability of these phases. In our plot, we show the energy of a distorted cF24 structure, which is mechanically stable, for comparison with the undistorted hP12

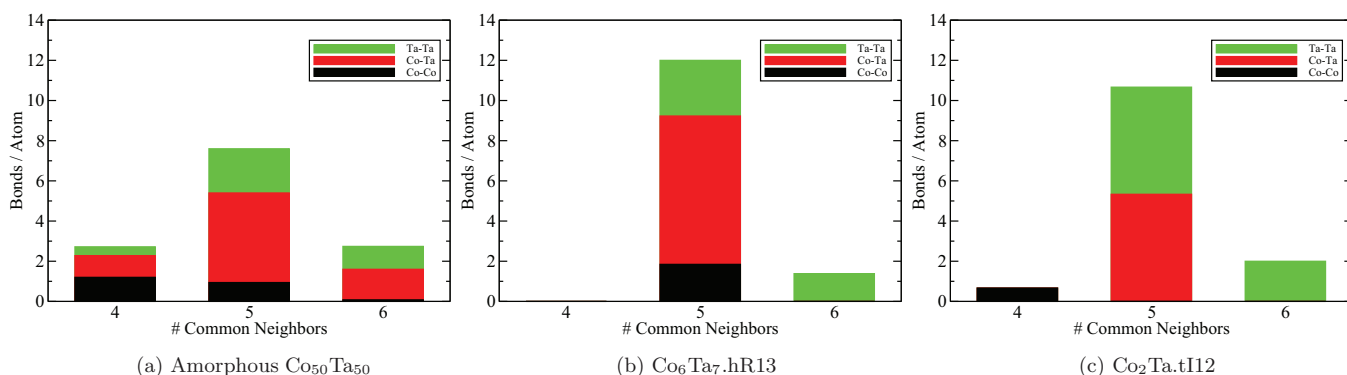


FIG. 3. (Color online) Stacked bar chart of Honeycutt-Andersen common neighbor statistics [39,40].

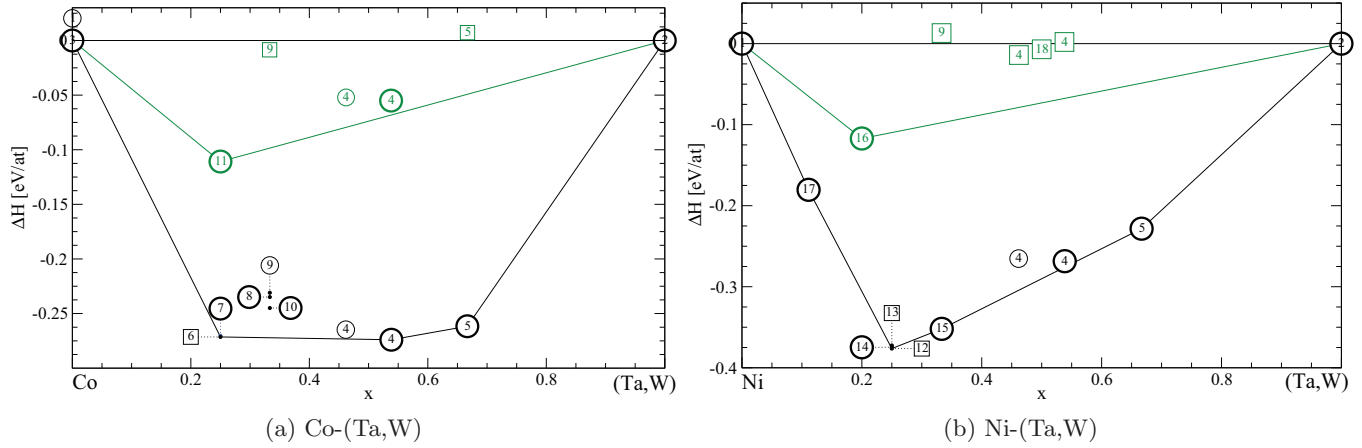


FIG. 4. (Color online) Enthalpies of formation for (Co,Ni)-(Ta,W) alloys. Values for Ta shown in black, for W shown in green. Plotting symbols explained in text.

and hP24. In the vicinity of $x = 0.5$ lies the Frank-Kasper μ phase. This phase is common to many alloy systems containing fourth and fifth row early transition metals with third row late transition metals. In most cases, the phase shows a broad composition range at high temperature but favors an ETM-rich low temperature limit (i.e., with the mixed occupancy $3a$ site occupied by an ETM). This feature is correctly reproduced by our calculation. At $x = 0.67$, the tI12 phase (reference number 5) is a noncanonical Frank-Kasper phase, as it contains a CN = 10 Bernal Hole, in addition to a canonical CN = 15 Kasper polyhedron.

2. Ni-Ta

For Ni-Ta [Fig. 4(b)] at $x = 0.11$ we find $\text{Ni}_8\text{Ta.tI18}$ to be low-temperature stable. The experimental phase diagram has a tI36 structure stable, however no crystallographic refinement exists, so we use the known tI18 phase instead. There is disagreement on recent phase diagrams concerning the stable structure at $x = 0.25$, and we find three different structures have nearly identical enthalpies (tI8 is the lowest). The main source of disagreement between our $T = 0$ K phase diagram and experimental phase diagrams is the stability of NiTa.hR13 , with even the ETM-rich variant lying 7 meV/atom above the convex hull. Figure 2 shows the diffraction patterns of our experimentally cast rods, verifying the existence of the expected phases in our own samples.

3. (Co,Ni)-W

Our calculations verify the known Co_3W and Ni_3W phase stabilities. However, the reported Co_7W_6 phase lies above the convex hull, and additionally favors the ETM-rich limit contrary to experimental report. This phase has not been reported in the Ni-W alloy system, and we indeed find it lies well above the convex hull. However, we will study the electronic and elastic properties of this hypothetical phase in order to elucidate trends with respect to composition. Notice that enthalpies of formation for alloys with W are lower than enthalpies with Ta. This does not necessarily reflect lower mechanical stability or melting points for the compounds, as the greater cohesive energy of tungsten compared to tantalum contributes to a reduction of the alloy formation enthalpies. An

equiatomic Ni-W phase with orthorhombic symmetry has been observed low-temperature stable [41], however, no atomic structural data exists. Owing to similar chemical identity and Bravais lattice, we attempted to use the Frank-Kasper phase MoNi.oP56 with Mo substituted for W, but found that this structure lies 66 meV/atom above the convex hull and likely is not the correct phase. It was also too computationally expensive to compute elastic moduli for this phase.

C. Binary elastic moduli

We examine the effect of alloying on the elastic moduli by using CPA to approximate a hypothetical alloy where no interspecies interactions exist. That is, for a well-ordered phase with stoichiometry $A_x B_{1-x}$, we compare its elastic moduli to a hypothetical solution of pure specie A and pure specie B with a stoichiometric ratio $x : (1 - x)$ in the CPA approximation. As input for CPA, we use our computed elemental elastic moduli. These agree closely with experimental moduli for Ta and W but are relatively high for Co and Ni. Note that our calculation are valid at 0 K, while the experimental values are room temperature, so it is expected that our values should be high, especially, for nonrefractory elements. As the CPA approximation only incorporates elemental elastic moduli with no atomic environmental details, the deviation of computed polycrystalline moduli from the CPA approximation yields a measure of the relative importance of atomic environment and alloying species for elastic moduli.

All crystal structures are elastically anisotropic, and it is of interest to characterize the anisotropy of our amorphous approximants. We define three anisotropies [20,42]: A_Z (Zener), A_G (shear), and A_E (Young's) as

$$A_Z = \frac{2C_{44}}{C_{11} - C_{12}}, \quad A_G = \frac{S_{44} + S_{66}}{2S_{44}},$$

and

$$A_E = \frac{S_{11}}{S_{33}},$$

all of which are 1 for isotropic structures, where S_{ij} are elements of the compliance matrix. Table II compares calculated anisotropies of our hR13 and tI12 structures with the four pure

TABLE II. Measures of anisotropy for materials of interest. $A_G = A_E = 1$ for cubic structures.

Composition	Structure	A_Z	A_G	A_E
Co-Ta	hR13	0.70	0.85	1.13
Ni-Ta	hR13	0.81	0.91	1.14
Co-W	hR13	0.76	0.88	1.18
Ni-W	hR13	1.12	1.06	1.45
Co-Ta	tI12	0.90	1.17	1.27
Ni-Ta	tI12	1.32	1.24	1.50
Co-W	tI12	1.24	1.12	1.20
Ni-W	tI12	1.42	1.16	1.07
Co	hP2	1.01	1.00	1.31
Ni	cF4	2.18	1	1
Ta	cI2	1.16	1	1
W	cI2	0.83	1	1

elements. Our anisotropies are close to one, similar to those seen in the pure metals, with hR13 exhibiting less anisotropy than tI12. These anisotropies can be taken as estimates of the local anisotropy expected at the atomic level in actual amorphous structures. Recall that the polycrystalline averages are expected to reflect the globally isotropic properties of the bulk amorphous structures.

Shown in Fig. 5 are our calculated K and G values, compared with CPA estimates. All CPA estimates are indicated by lines, all calculated moduli by individual data points, and for Ni-Ta asterisks indicate experimental results. Our calculated Ni-Ta bulk moduli show excellent agreement with our experimental results. For all four chemical families, CPA gives reasonable estimates for bulk moduli, with at most a 16% deviation between estimated and calculated bulk moduli. However, in all alloy systems and for all structures examined, CPA underestimates the bulk modulus. This suggests the dominant correction to the bulk moduli is chemical bonding and not atomic environmental details such as the prevalence of tetrahedra. Shear moduli show relatively larger and less regular deviations from CPA, suggesting that bond topology plays

a significant role. Nonetheless, our calculated Ni-Ta shear moduli are in good agreement with experiment (crosses).

Shown in Table III are the correlation coefficient for various linear regressions across all calculated CoTa, CoW, NiTa, and NiW alloys, where the sign of the correlation coefficient denotes the sign of the slope. Here, ΔK and ΔG (units GPa) are deviations of calculated bulk and shear moduli from CPA estimates, Δv (units \AA^3 per atom) the deviation of volume per atom from a linear interpolation of pure elements, and Δh (units eV per atom) the enthalpy of formation per atom as illustrated in Fig. 4. Correlations of elastic moduli with Δv and Δh reflect structure and bonding effects that are missing from CPA. There is only a weak correlation between Δh and Δv , though the associated slope is positive, expected as increased bond strength (more negative Δh) draws atoms closer together (more negative Δv). ΔG and ΔK are both correlated to Δv , with ΔK , in particular, strongly correlated. This is in line with other work that shows that K and G correlate with V and that the correlation for K is particularly strong [9]. This is also true for individual chemical families, and for ΔK all chemical families' regressions have similar slopes. This strong correlation of ΔK with Δv explains why all structures have CPA underestimating the bulk moduli (positive ΔK), as all structures were also observed to have negative Δv , as expected. The slopes of ΔG and ΔK are both negative, as decreasing Δv draws atoms closer together, shortening bonds and enhancing interatomic force constants. The observed correlation of ΔG with ΔK is likely due to the underlying correlation of each with Δv .

A goal of metallic glass design is to predict glass-forming compounds with high ductility. Thus, as a guide, we plot the Poisson ratio's of the various alloys under discussion in Fig. 6. Our computed $T = 0$ K crystalline Poisson ratios are expected to be systematically low relative to the corresponding glasses, as G decreases more rapidly than K as temperature increases [43], and amorphous G and K are lower relative to crystalline values by around 30% and 10%, respectively. Here, we see no systematic trend in the choice of Ta versus W (empty versus filled plotting symbols) but Ni generally has

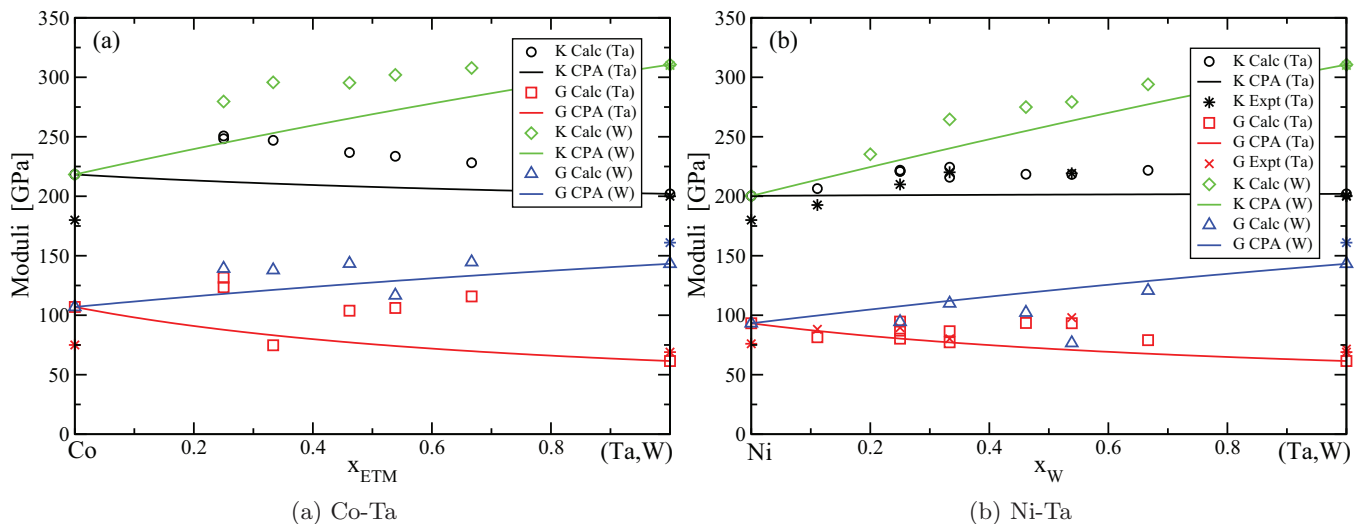


FIG. 5. (Color online) Elastic moduli for (Co,Ni)-(Ta,W) compounds. Lines show CPA estimates. Data points are our DFT calculations. Asterisks are experimental values from our experiments on Ni-Ta alloys and from the literature for pure elements.

TABLE III. Correlation coefficients for linear regressions involving elastic moduli and thermodynamic quantities of interest, where rows denote independent variables and columns dependent variables for a given regression.

	Δv	Δh	ΔK	ΔG
Δv	...	0.20	-0.83	-0.66
Δh	0.20	...	0.06	-0.47
ΔK	-0.83	0.06	...	0.60
ΔG	-0.66	-0.47	0.60	...

higher Poisson's ratio than Co (red versus blue). Empirically, it has been observed that $\nu = 0.32$ serves as a rough criterion for separating ductile and brittle behavior in amorphous materials [6]. The majority of our Ni alloys lie above this criterion and Co alloys below. In particular, all Ni-W alloys satisfy this criterion, and Ni-W in the amorphous approximant structure hR13 shows particularly large Poisson's ratios. Combined with the large bulk modulus due to the presence of tungsten, we propose that Ni-W is a candidate system for future research into strong amorphous materials with high ductility.

IV. ANALYSIS AND DISCUSSION

To understand trends in elastic constants of these alloys, we now look into the interatomic interactions. Within a first-principles approach there is no unique decomposition of interactions into pairwise and many-body forces, and no simple notion of a chemical bond, especially for metals. However, some heuristic measures are available. Here, we examine the interatomic force constants, which can be regarded as springs connecting the atoms, and the crystal overlap Hamilton populations (COHPs), which are a measure of the covalency of electronic wave functions.

A. Force constants and COHP

To compare different ETM and LTM substitutions, Table IV shows k , the mean force constants for the near neighbor bonds of a given species combination, ρ_{COHP} , the total iCOHP per unit volume for bonds of a given species combination up to 4 Å, and K , the bulk moduli in the structural prototype tI12. To calculate the mean force constant, we sum force constants for all bonds up to 4 Å for a given cell then divide by the number of atoms.

Both the mean force constant and ρ_{COHP} correlate with the bulk moduli. This is especially notable in the mean force constant, where there is a large increase in mean force constant

TABLE IV. Data for tI12. R are average bond lengths for nearest neighbors under 4 Å. k are averaged over atoms (i.e., weighted by the number of bonds per atom) in units $\text{eV}/\text{\AA}^2$, ρ_{COHP} is iCOHP volume density in units $\text{eV}/\text{\AA}^3$, and K is the calculated bulk moduli in units GPa.

Compound	ETM-ETM (44x)			ETM-LTM (32x)			LTM-LTM (4x)			mean	mean	K
	R	k	ρ_{COHP}	R	k	ρ_{COHP}	R	k	ρ_{COHP}	k	ρ_{COHP}	
NiTa ₂	3.12	4.2	0.31	2.63	4.7	0.25	2.43	4.2	0.025	30.7	0.27	222
CoTa ₂	3.11	5.2	0.31	2.61	3.7	0.30	2.48	4.0	0.030	32.0	0.29	228
NiW ₂	3.02	4.0	0.31	2.55	7.6	0.34	2.38	4.3	0.041	37.7	0.31	294
CoW ₂	3.02	5.1	0.37	2.54	6.7	0.36	2.38	4.8	0.037	39.9	0.35	308

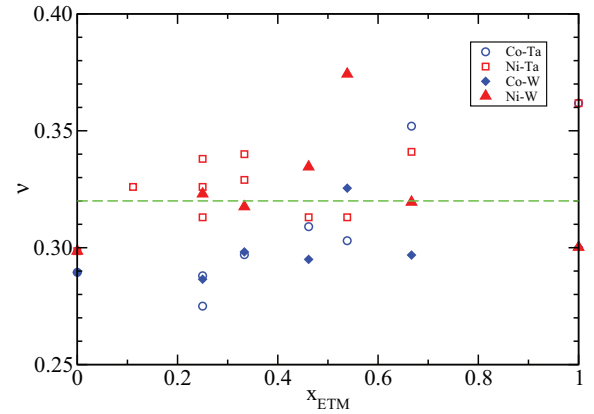


FIG. 6. (Color online) Calculated Poisson ratios. Dashed line at $\nu = 0.32$ is putative threshold for ductility.

performing a Ta \rightarrow W substitution and a relatively small increase performing a Ni \rightarrow Co substitution, but the effect is also present in ρ_{COHP} . As a force constant gives a measure of the stiffness of an individual bond, this mean force constant gives a measure of the total stiffness of all bonds, and bulk modulus is increased under chemical substitution by an overall increase in the interatomic force constant. We also see in Table IV that performing a Ni \rightarrow Co or a Ta \rightarrow W substitution enhances ρ_{COHP} . Thus these substitutions have enhanced the bonding nature of the electronic states.

To further understand the enhancement of bonding, we calculate electronic densities of state (Fig. 7). The low-energy peak near -4 or -5 eV consists of sd -hybrid orbitals, followed by a series of higher-energy peaks consisting solely of d orbitals, with the Fermi level lying in the middle of the ETM d band and at or above the top of the LTM d band. For Co-W, the Co and W d bands are closely aligned, inducing strong hybridization of Co and W d orbitals. This effect is present in all structural prototypes we have examined. Performing a W \rightarrow Ta substitution shifts the ETM d band up relative to the LTM d band, decreasing the d -band overlap and diminishing hybridization. Performing a Co \rightarrow Ni substitution shifts the LTM d band down relative to the ETM d band, also decreasing the d -band overlap. Both of these induce an decrease in the hybridization of the ETM-LTM d bands. As hybridization generally creates bonding states below the Fermi level, this reduction in hybridization going from W \rightarrow Ta and Co \rightarrow Ni decreases the overall bonding characteristic of the occupied states, leading to the observed trends in ρ_{COHP} , and hence in bulk modulus.

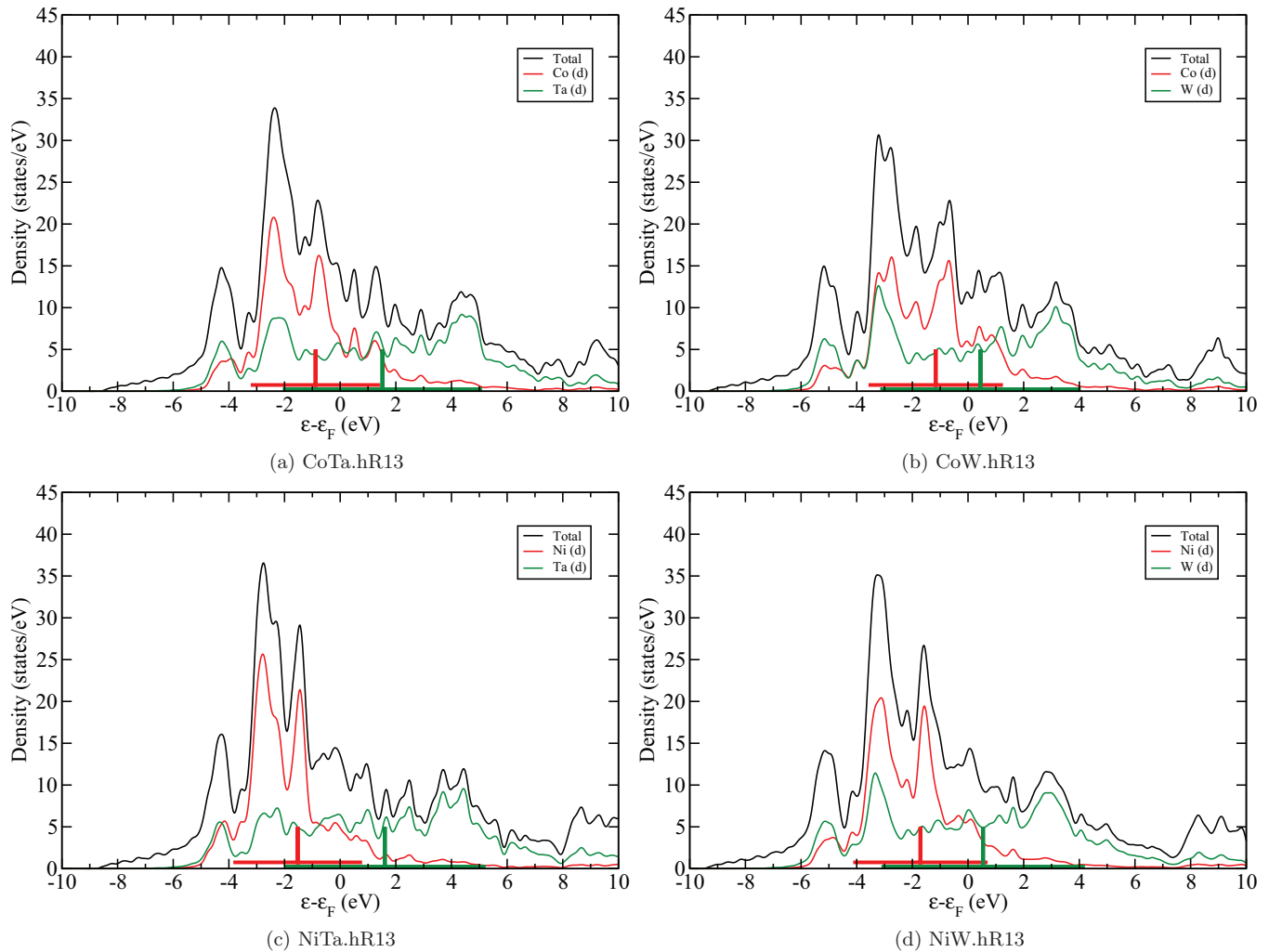


FIG. 7. (Color online) Electronic densities of states for hR13 structures. Line segments indicate the mean and standard deviations of the element projected d bands.

B. Microstructural details: ternaries and quaternaries

Elemental properties provide the dominant contribution to the elasticity of these ETM-LTM intermetallic compounds, as can be seen in the qualitative agreement of calculated alloy moduli with the CPA predictions shown in Fig. 5. In Table V we see that the small decreases in modulus from Co to Ni, and the large increases from Ta to W, are echoed in the moduli of the hR13 Frank-Kasper structure.

While binary amorphous metals exist, size mismatch criteria and material property tuning favor the usage of multiple constituent species in amorphous metals for practical

TABLE V. Elastic moduli for pure elements and binary hR13 structures.

		K	G		K	G
	Co	218	107	Ni	200	93
Nb ($K = 173, G = 22$)	Co ₆ Nb ₇	213	92	Ni ₆ Nb ₇	198	81
Ta ($K = 202, G = 61$)	Co ₆ Ta ₇	234	106	Ni ₆ Ta ₇	218	93
W ($K = 331, G = 143$)	Co ₆ W ₇	302	117	Ni ₆ W ₇	279	77

applications, and thus the question of transferability of binary results to structures with three or more constituent species must be addressed. In addition, there is still the lingering need to quantify how atomic environment affects the elastic moduli. To answer both these questions, we perform chemical substitutions in a binary structure to yields ternaries and quaternary structures. This changes the chemical identities of formerly equivalent sites, altering local chemical ordering.

Shown in Table VI is a comparison of binary hR13 structures (including also alloys with Nb, an ETM) with nearly equiatomic quaternary variants of hR13 and six associated ternaries. Site occupancies in the quaternary has been chosen to maintain the ETM/LTM nature of sites and minimize energy, and the ternaries were formed by keeping the early/late site identity fixed.

To compare our binary results to ternaries and quaternaries, we here use a simple chemical environment averaging scheme between ETM and LTM, with a equiatomic $ABCD$ mixture with A and B LTM and C and D ETM approximated by $1/4(AC + AD + BC + BD)$, and an ABC mixture (with C having near 50% concentration) approximated by $1/2(AC + BC)$. Here, AC , AD , BC , and BD refer to the relevant binary

TABLE VI. Comparison of calculated ternary and quaternary hR13 moduli with averaged values of binaries. Moduli are given in GPa, and deviations in percentages.

Chemical formula	Calculated K, G	Averaged K, G	Deviation
$\text{Co}_3\text{Ni}_3\text{Nb}_7$	205, 87	205, 87	0.3, 0.5
$\text{Co}_3\text{Nb}_3\text{Ta}_4$	225, 100	223, 99	0.7, 1.4
$\text{Co}_3\text{Ni}_3\text{Ta}_7$	225, 102	226, 100	0.4, 2.2
$\text{Ni}_6\text{Nb}_3\text{Ta}_4$	210, 89	208, 87	0.9, 2.2
$\text{Co}_3\text{Ni}_3\text{W}_7$	290, 94	291, 97	0.3, 2.4
$\text{Co}_3\text{Ni}_3\text{Nb}_3\text{Ta}_4$	217, 97	216, 93	0.1, 3.7
$\text{Co}_6\text{Ta}_4\text{W}_3$	261, 123	268, 111	2.5, 10.0
$\text{Co}_3\text{Ni}_3\text{Ta}_3\text{W}_4$	253, 115	258, 98	2.1, 14.6
$\text{Co}_6\text{Nb}_3\text{W}_4$	261, 121	257, 104	1.5, 16.4
$\text{Ni}_6\text{Nb}_3\text{W}_4$	241, 92	239, 79	0.8, 16.8
$\text{Ni}_6\text{Ta}_4\text{W}_3$	242, 100	249, 85	2.6, 17.8
$\text{Co}_3\text{Nb}_3\text{Ni}_3\text{W}_4$	248, 109	248, 92	0.2, 18.7

hR13 structure with the associated chemical formula. As an example, the predicted bulk moduli of $\text{Co}_6\text{Ta}_3\text{W}_4$ would be the average bulk modulus of Co_6Ta_7 and Co_6W_7 . While this ignores interspecies ETM-ETM and LTM-LTM bonds present (i.e., *AB* and *CD*), binary enthalpies of formation for ETM-ETM and LTM-LTM families are weak compared to ETM-LTM families, suggesting that as a first approximation we may assume the differences in interspecies ETM-ETM and LTM-LTM bond strength average out.

Differences between our predicted interpolated elastic moduli and computed elastic moduli follow the trends previously reported for CPA. Again, we see bulk moduli negligibly affected by atomic environment and predominately determined by the alloying species, with deviations in bulk moduli below 2.6% for all structures. For shear moduli, the structures can be placed into two categories: those structures that have only one ETM species or else two ETM species from the same group (here Nb and Ta belong to group IV), which have deviations in shear moduli below 3.7%, and those that have ETM species from different groups (here W from group V together with Nb or Ta from group IV) which have deviations in shear moduli between 10.0% and 18.7%. In all cases where predicted shear

moduli deviate significantly from calculated shear moduli, the computed shear moduli have been enhanced.

That mixing Co and Ni or Nb and Ta causes little deviation in shear modulus, but mixing Ta and W does, is further evidence for the dependence of shear modulus on atomic environment. Co and Ni have similar atomic radii and electronegativity, as do Nb and Ta. For a topologically close-packed structure like hR13, substitution of these chemical species should not noticeably affect bond lengths and ionic charges, yielding similar calculated and averaged results. However, Nb and Ta have larger atomic radii and lower electronegativity than W, leading to larger charge transfers and changes in bond length, reducing the accuracy of our averaging scheme, while generally increasing bonding strength.

V. CONCLUSIONS

In this paper, we examined the elasticity of various early transition metal-late transition metal crystalline binary alloys using first-principles calculations and comparison with various averaging schemes. Calculated bulk moduli were reasonably close to the CPA using pure elemental species, but CPA predictions were systematically low. This deviation correlates strongly with volume per atom. Larger and less regular deviations were observed for shear moduli, suggesting structural distortion being responsible for the deviation. Select ternary and quaternary structures were examined and confirmed these trends. To explain the dependence of elastic moduli on chemical bonding, force constants and electronic densities of state were calculated and it was found early transition metals are responsible for the strongest bonding, which agrees with observed trends in the bulk moduli. We find that Ni-W alloys have the largest Poisson ratios among the compositions studied and hence hold promise as the basis for design of ductile metallic glasses.

ACKNOWLEDGMENT

We would like to give special thanks to DOD-DTRA for funding this research under contract number DTRA-11-1-0064.

-
- [1] T. Egami, *Mat. Sci. Eng. A* **226-228**, 261 (1997).
 - [2] T. Egami, S. J. Poon, Z. Zhang, and V. Keppens, *Phys. Rev. B* **76**, 024203 (2007).
 - [3] W. H. Wang, *J. Appl. Phys.* **99**, 093506 (2006).
 - [4] S. J. Poon, A. Zhu, and G. J. Shiflet, *Appl. Phys. Lett.* **92**, 261902 (2008).
 - [5] H. S. Chen, J. T. Krause, and E. Coleman, *J. Non-Cryst. Solids* **18**, 157 (1975).
 - [6] J. J. Lewandowski, W. H. Wang, and A. L. Greer, *Philos. Mag. Lett.* **85**, 77 (2005).
 - [7] J. Q. Wang and H. Y. Bai, *Scripta Mater.* **61**, 453 (2009).
 - [8] W. L. Johnson and K. Samwer, *Phys. Rev. Lett.* **95**, 195501 (2005).
 - [9] W. H. Wang, *Prog. Mater. Sci.* **57**, 487 (2012).
 - [10] F. C. Frank and J. S. Kasper, *Acta Cryst.* **11**, 184 (1958).
 - [11] F. C. Frank and J. S. Kasper, *Acta Cryst.* **12**, 483 (1959).
 - [12] A. K. Sinha, *Prog. Mater. Sci.*, **15**(2) 81 (1972).
 - [13] M. Telford, *Mater. Today* **7**, 36 (2004).
 - [14] C. C. Hays, C. P. Kim, and W. L. Johnson, *Phys. Rev. Lett.* **84**, 2901 (2000).
 - [15] L. D. Landau and E. M. Lifshitz, *Theory of Elasticity*, Course of Theoretical Physics, 3rd ed. (Butterworth-Heinemann, Burlington, MA, USA, 1986), Vol. 7.
 - [16] S. F. Pugh, *Philos. Mag.* **45**, 823 (1954).
 - [17] X. J. Gu, A. G. McDermott, S. J. Poon, and G. J. Shiflet, *Appl. Phys. Lett.* **88**, 211905 (2006).
 - [18] A. Inoue, B. Shen, H. Koshiba, H. Kato, and A. R. Yavari, *Nat. Mater.* **2**, 661 (2003).
 - [19] M. Ohtsuki, R. Tamura, S. Takeuchi, S. Yoda, and T. Ohmura, *Appl. Phys. Lett.* **84**, 4911 (2004).

- [20] J. F. Nye, *Physical Properties of Crystals: Their Representation by Tensors and Matrices*, 2nd ed. (Oxford Science Publications, New York, NY, USA, 1985).
- [21] R. Zeller and P. H. Dederichs, *Phys. Status Solidi B* **55**, 831 (1973).
- [22] R. Hill, *Proc. Phys. Soc. A* **65**, 349 (1952).
- [23] C. W. Nan, *Prog. Mater. Sci.* **37**, 1 (1993).
- [24] Y. Zhang and A. L. Greer, *J. Alloys Compd.* **434-435**, 2 (2007).
- [25] B. Zhang, R. J. Wang, D. Q. Zhao, M. X. Pan, and W. H. Wang, *Phys. Rev. B* **73**, 092201 (2006).
- [26] G. Kresse and J. Hafner, *Phys. Rev. B* **47**, 558(R) (1993).
- [27] G. Kresse and J. Furthmüller, *Phys. Rev. B* **54**, 11169 (1996).
- [28] P. E. Blöchl, *Phys. Rev. B* **50**, 17953 (1994).
- [29] J. P. Perdew and Y. Wang, *Phys. Rev. B* **45**, 13244 (1992).
- [30] M. Mihalkovic and M. Widom, *Phys. Rev. B* **70**, 144107 (2004).
- [31] R. Dronskowski and P. E. Blöchl, *J. Phys. Chem.* **97**, 8617 (1993).
- [32] O. Jepsen and O. K. Andersen, *Z. Phys. B* **97**, 35 (1995).
- [33] A. Migliori and J. L. Sarrao, *Resonant Ultrasound Spectroscopy* (Wiley, New York, NY, USA, 1997).
- [34] H. W. Sheng, W. K. Luo, F. M. Alamgir, J. M. Bai, and E. Ma, *Nature (London)* **439**, 419 (2006).
- [35] X. W. Fang, C. Z. Wang, S. G. Hao, M. J. Kramer, Y. X. Yao, M. I. Mendelev, Z. J. Ding, R. E. Napolitano, and K. M. Ho, *Sci. Rep.* **1**, 194 (2011).
- [36] J. D. Bernal, *Proc. R. Soc. Lond. A* **280**, 299 (1964).
- [37] D. R. Nelson, *Phys. Rev. B* **28**, 5515 (1983).
- [38] D. B. Miracle, *JOM* **64**, 846 (2012).
- [39] J. D. Honeycutt and H. C. Andersen, *J. Phys. Chem.* **91**, 4950 (1987).
- [40] P. Ganesh and M. Widom, *Phys. Rev. B* **77**, 014205 (2008).
- [41] J. M. Walsh and J. M. J. Donachie, *Met. Trans.* **4**, 2854 (1973).
- [42] D. Tromans, *Int. J. Res. Rev. Appl. Sci.* **6**(4), 462 (2011).
- [43] X. F. Liu, R. J. Wang, and W. H. Wang, *Scripta Mater.* **62**, 254 (2010).